

---

**Supplementary information**

---

**Direct growth of single-metal-atom chains**

---

In the format provided by the  
authors and unedited

# Supplementary Information

## Direct growth of single-metal-atom chains

Shasha Guo, Jiecai Fu, Peikun Zhang, Chao Zhu, Heming Yao, Manzhang Xu, Boxing An, Xingli Wang, Bijun Tang, Ya Deng, Teddy Salim, Hongchu Du, Rafal E. Dunin-Borkowski, Mingquan Xu, Wu Zhou, Beng Kang Tay, Chao Zhu, Yanchao He, Mario Hofmann, Ya-Ping Hsieh, Wanlin Guo, Michael Ng, Chunlin Jia\*, Zhuhua Zhang\*, Yongmin He\*, and Zheng Liu\*

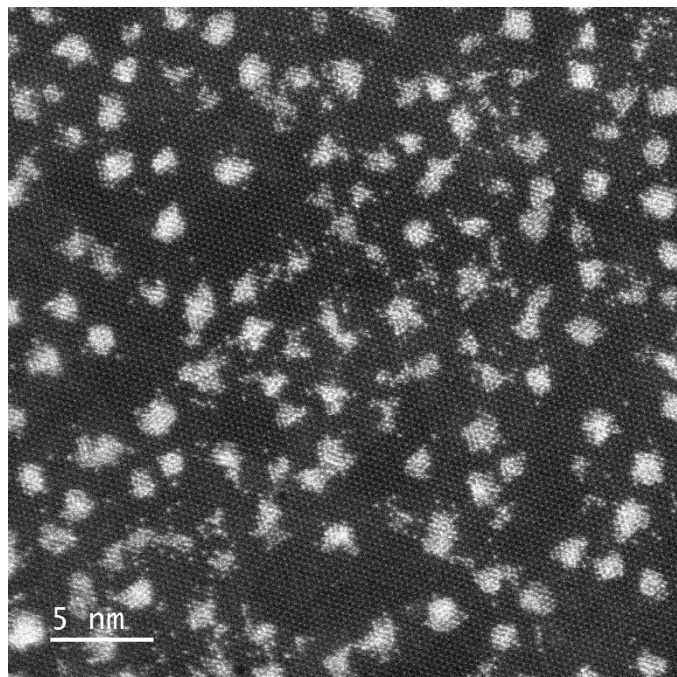
\*Correspondence to: [c.jia@fz-juelich.de](mailto:c.jia@fz-juelich.de), [chuwazhang@nuaa.edu.cn](mailto:chuwazhang@nuaa.edu.cn), [ymhe@hnu.edu.cn](mailto:ymhe@hnu.edu.cn), and [z.liu@ntu.edu.sg](mailto:z.liu@ntu.edu.sg)

## Table of contents

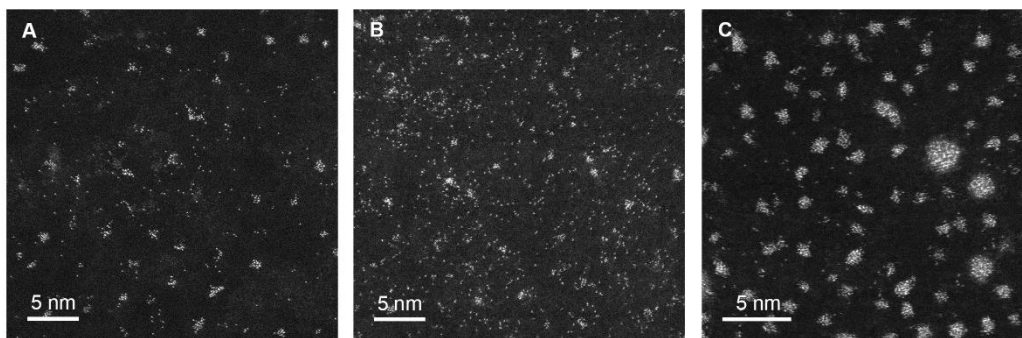
S1	Synthesis and structural characterization of Pt SMACs in MoS <sub>2</sub> film .....	4
	Supplementary Fig. 1 Atomically resolved STEM image of Pt clusters just evaporated onto MoS <sub>2</sub> substrate. ....	4
	Supplementary Fig. 2 Monodispersed Pt single atom/nanoclusters on graphene.....	5
	Supplementary Fig. 3 Chemical vapor co-deposition process for the growth of Pt SMACs. ....	6
	Supplementary Fig. 4 HAADF STEM characterizations of materials grow under different condition. ....	7
	Supplementary Fig. 5 Atomic-resolution STEM-d energy-dispersive X-ray spectroscopy (EDX) of Pt SMACs in MoS <sub>2</sub> nanograin film. ....	8
	Supplementary Fig. 6 XPS characterizations of the Pt SMACs in MoS <sub>2</sub> nanograin film. .	9
	Supplementary Fig. 7 Pt : Mo atoms ratio counting. ....	10
	Supplementary Fig. 8 Massive atom-resolved ADF-STEM images verifying the general condition of Pt SMACs in our fabricated samples.....	11
	Supplementary Fig. 9 STEM investigation of Pt distribution in grain boundaries of small twist angle in Pt SMACs in MoS <sub>2</sub> nanograin films. ....	12
	Supplementary Fig. 10 Intensity profile along white lines in Fig. 2b-c .....	13
	Supplementary Fig. 11 Atomic structure of vertex areas and joints of Pt SMACs.....	14
	Supplementary Fig. 12 STEM investigation of Pt SMACs across monolayer and bilayer MoS <sub>2</sub> . ....	15
	Supplementary Table 1. Raman spectra obtained from MoS <sub>2</sub> films. ....	16
S2	Investigation of the possible growth mechanism.....	17
	2.1 Ab initio molecular dynamic (MD) simulations for Pt SMACs in bilayer MoS <sub>2</sub> .....	17
	Supplementary Fig. 13 Binding energy of Pt atoms on monolayer MoS <sub>2</sub> .....	18
	Supplementary Fig. 14 Formation energy of different Pt SMACs configuration in monolayer MoS <sub>2</sub> nanograin film.....	19
	Supplementary Fig. 15 MD model for Pt SMACs in bilayer MoS <sub>2</sub> after structure optimization. ....	20
	Supplementary Fig. 16 The energy pathways for the kinetic growth along the Pt-passivated edge. ....	21
	Supplementary Fig. 17 The widths of electronic bands derived from incorporated Pt atoms in MoS <sub>2</sub> as a function of the Pt-Pt spacing in the system. ....	22
	Supplementary Fig. 18 Co SMACs in MoS <sub>2</sub> . ....	23
S3	Electronic structure study and thermal stability investigation.....	24

Supplementary Fig. 19 Thermal stability at 1000K.....	<b>24</b>
Supplementary Fig. 20 Projected density-of-states (PDOS).....	<b>25</b>
Supplementary Fig. 21 Electron localization function (ELF) map of Pt SMACs in a monolayer MoS <sub>2</sub> on the (001) pane.. .....	<b>26</b>
Supplementary Fig. 22 Optical microscope image (A) and zoom in SEM image (B) of FET devices in a TLM structure defined using e-beam lithography.....	<b>27</b>
Supplementary Fig. 23 Electrical measurments.....	<b>28</b>
Supplementary Fig. 24 FET performance of CVD-grown single crystal MoS <sub>2</sub> on SiO <sub>2</sub> substrate. ....	<b>29</b>
Supplementary Fig. 25 Complex network modelling Pt SMAC inside MoS <sub>2</sub> film.. .....	<b>30</b>
Supplementary Note 1 Discussion of liquid Pt nanodroplets. ....	<b>31</b>
Supplementary Note 2 Discussion on network conduction mechanism.....	<b>32</b>
Supplementary Note 3 Discussion on the controbility of Pt SMACs.....	<b>33</b>
S4 References.....	<b>34</b>

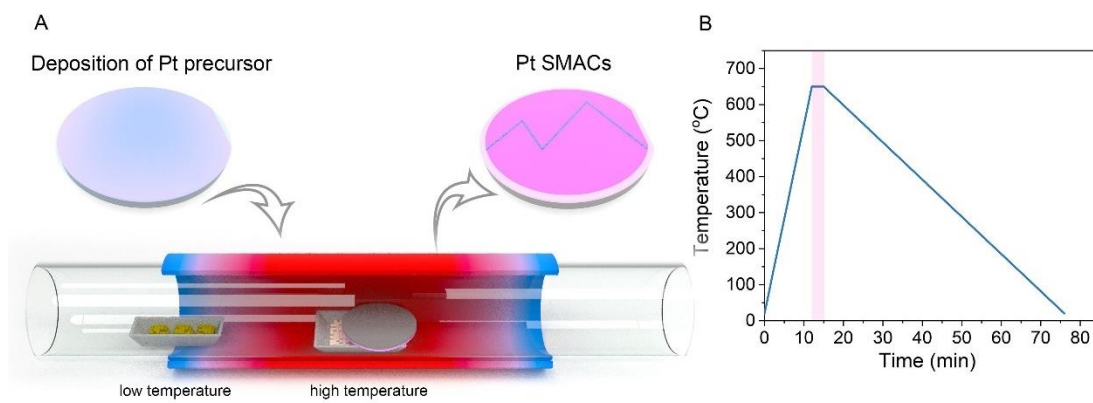
## S1 Synthesis and structural characterization of Pt SMACs in MoS<sub>2</sub> film



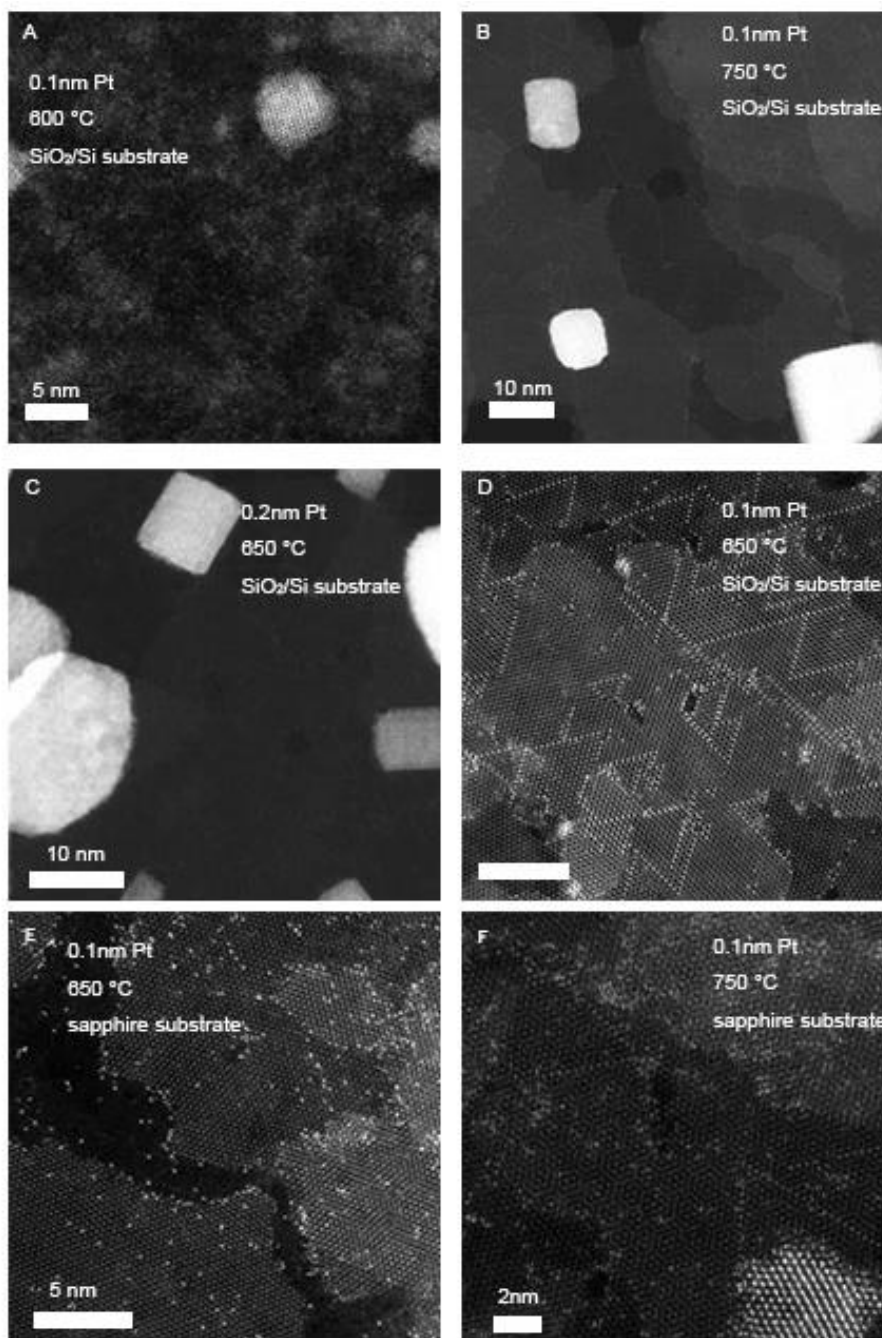
**Supplementary Fig. 1 | Atomically resolved STEM image of Pt clusters just evaporated onto MoS<sub>2</sub> substrate. The size of Pt cluster is about 0.5-2 nm.**



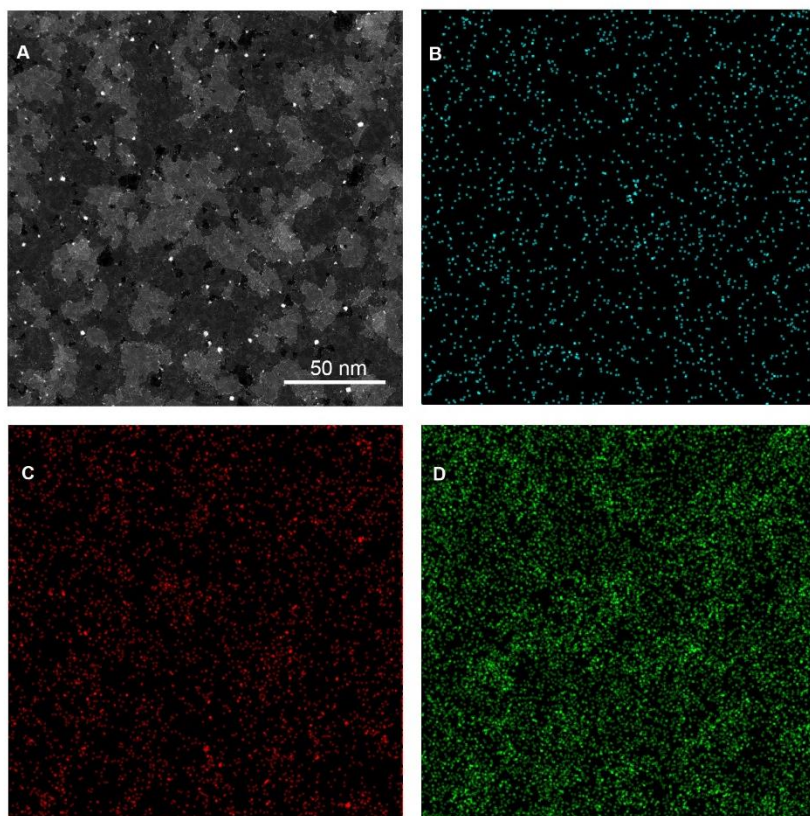
**Supplementary Fig. 2 | Monodispersed Pt single atom/nanoclusters on graphene.** A-C Atomically resolved STEM image of the distribution of Pt species just evaporated onto graphene substrate as increasing the deposition time at a rate of  $0.1 \text{ \AA/s}$ . A 1 s, B 2 s, C 10 s.



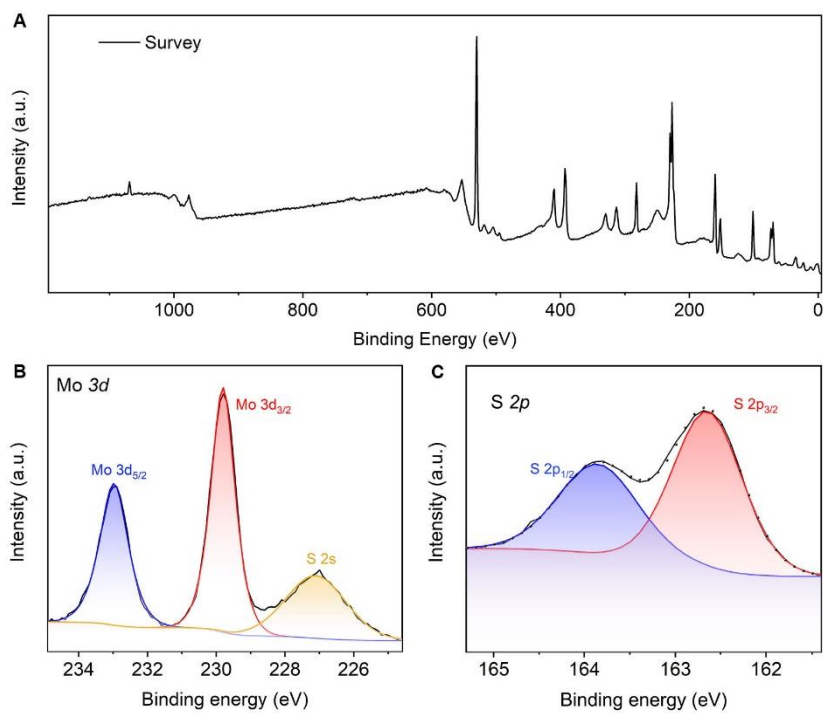
**Supplementary Fig. 3 | Chemical vapor co-deposition process for the growth of Pt SMACs.** (A) The Schematic diagram of CVD setup. (B) The temperature profile of MoO<sub>3</sub> and Pt nanocluster coated substrate.



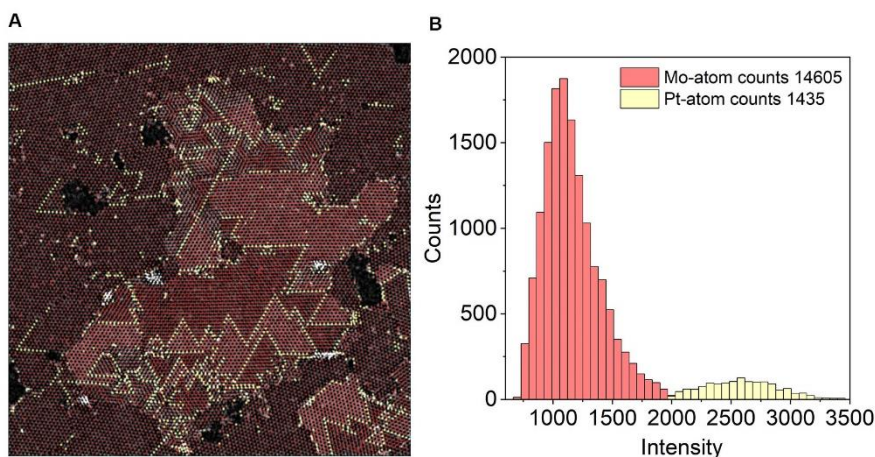
**Supplementary Fig. 4 | HAADF STEM characterizations of materials grow under different condition.** (A) STEM images of single Pt atoms in amorphous MoS<sub>2</sub> film under growth condition of 0.1nm Pt coated SiO<sub>2</sub>/Si substrate and 600 °C. (B) STEM images of Pt SMACs/PtS<sub>x</sub> nanoparticles in MoS<sub>2</sub> nanograin film under growth condition of 0.1nm Pt coated SiO<sub>2</sub>/Si substrate and 750 °C. (C) STEM images of Pt SMACs/Pt nanoparticles in MoS<sub>2</sub> nanograin film under growth condition of 0.2nm Pt coated SiO<sub>2</sub>/Si substrate and 650 °C. (D) STEM images of Pt SMACs in MoS<sub>2</sub> nanograin film under growth condition of 0.1nm Pt coated SiO<sub>2</sub>/Si substrate and 650 °C. (E) STEM images of single Pt atom doped MoS<sub>2</sub> nanograin film under growth condition of 0.1nm Pt coated sapphire substrate and 650 °C. (F) STEM images of single Pt atoms/Pt SMACs/PtS<sub>x</sub> nanoparticles in MoS<sub>2</sub> nanograin film under growth condition of 0.1nm Pt coated sapphire substrate and 750 °C.



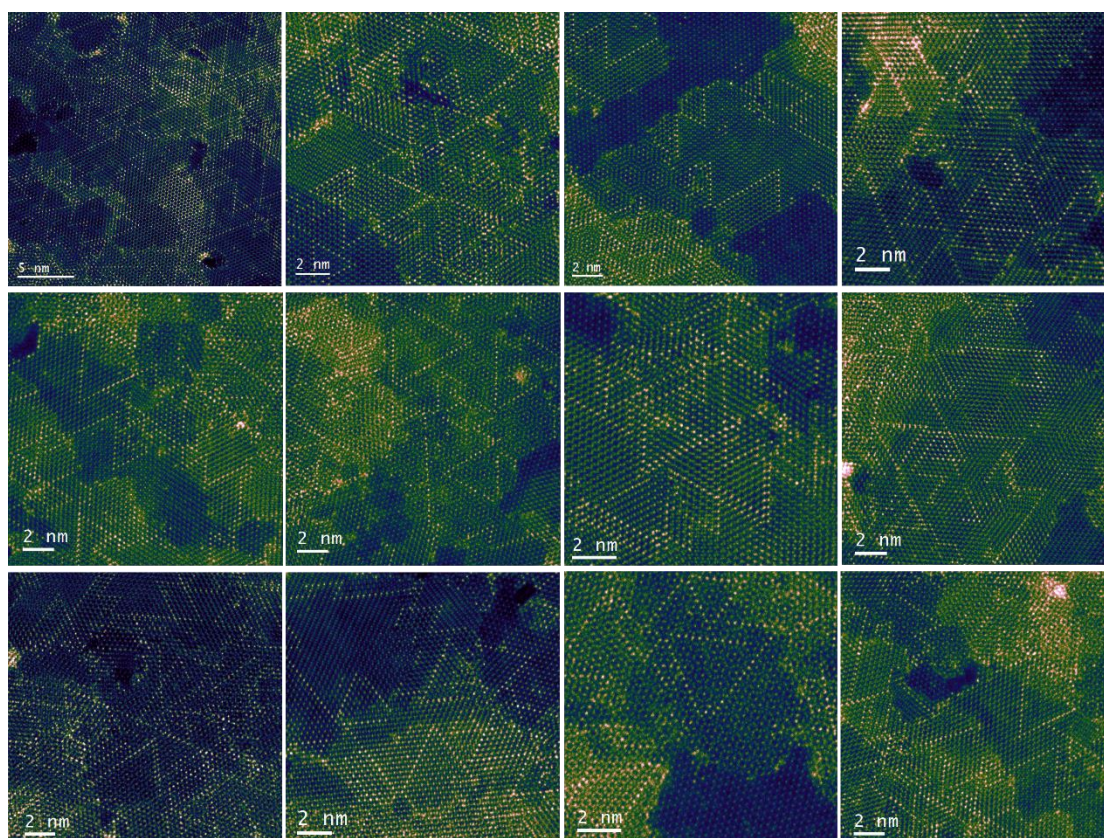
**Supplementary Fig. 5 | Atomic-resolution STEM-d energy-dispersive X-ray spectroscopy (EDX) of Pt SMACs in MoS<sub>2</sub> nanograin film.** (A) low magnification STEM images of materials for growth condition of SiO<sub>2</sub>/Si substrate and 650 °C. (B-D) STEM-EDX elemental maps of Mo (B), Pt (C), and S (D).



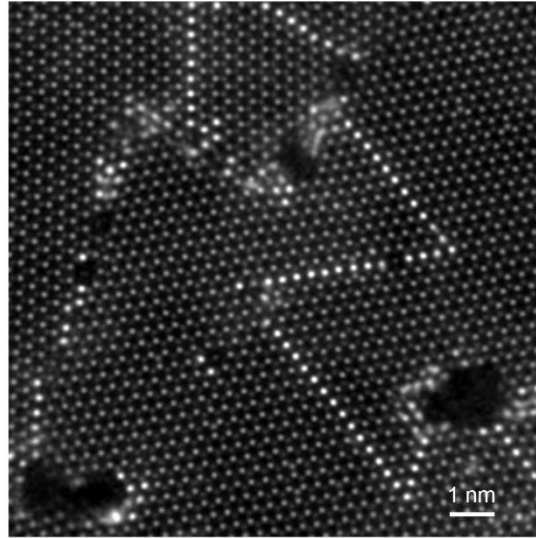
**Supplementary Fig. 6 | XPS characterizations of the Pt SMACs in MoS<sub>2</sub> nanograin film.** (A) Survey. (B) Mo 3d, where the binding energy at 229.8 and 233 eV can be attributed to the doublet Mo 3d<sub>3/2</sub> and Mo 3d<sub>5/2</sub>. (C) S 2p, where a set of peaks can be identified at 162.64 eV and 163.58 eV, assigned to S 2p<sub>3/2</sub> and S 2p<sub>1/2</sub>.



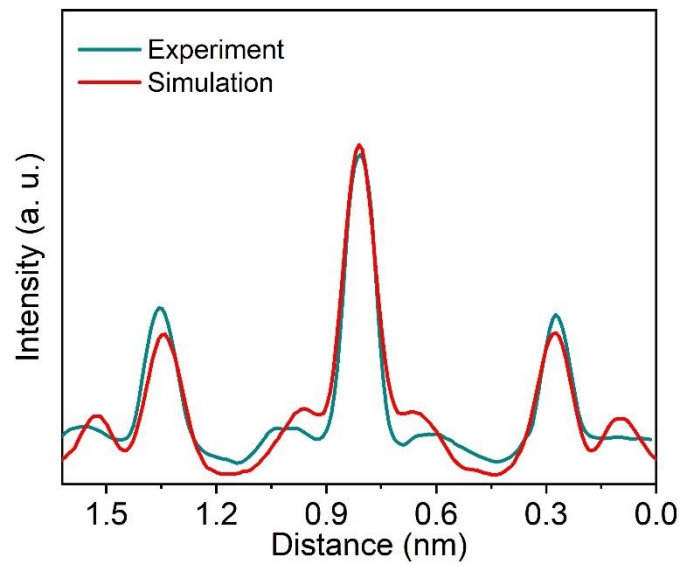
**Supplementary Fig. 7 | Pt : Mo atoms ratio counting.** (A) Color marked HAADF-STEM image of large-scale FOV (field of view) with the single-layer and bilayer region in Pt SMACs/MoS<sub>2</sub> nanograin film, Mo in red, Pt in yellow. (B) Histogram of scattered intensities of Pt and Mo atom columns in b. Only the cation sites were mapped since the Pt-dispersion occurs only in the cation sites. During the atom-atom mapping process, the intensity of each atomic column was fitted with a 2D Gaussian profile, which reflects the atom species due to the Z-contrast nature of HAADF-STEM imaging (i.e., the HAADF-STEM image intensity is linear to  $Z^{1.7}$ , Z denotes the atomic number). The 2D Gaussian fitting was performed with the multi-ellipse shaped profile using the package CalAtom developed by Lin et al.<sup>1</sup> It is worth noting that the intensity distribution of each atomic column is a broad Gaussian peak instead of a sharp delta function, in which the variance is affected to some extent by the peak finding and calculation errors, the aberration condition of the electron probe, inhomogeneously distributed absorbates or surface contamination, etc., but different chemical species between the Mo and Pt can still be distinguished on a statistical level when their atomic weight differs. Accordingly, the distribution of Pt and Mo atoms can be colored with yellow and red dots in the HAADF-STEM image, and a statistical result reveals that **the atom ratio of Pt and Mo** in the sample is about **1:10**.



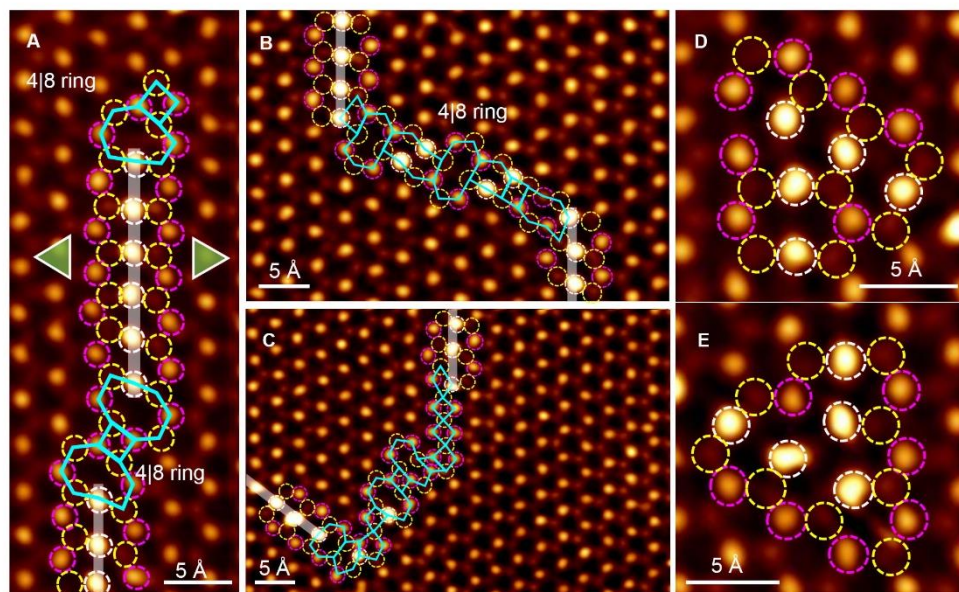
**Supplementary Fig. 8 | Massive atom-resolved ADF-STEM images verifying the general condition of Pt SMACs in our fabricated samples, which were recorded from several samples.**



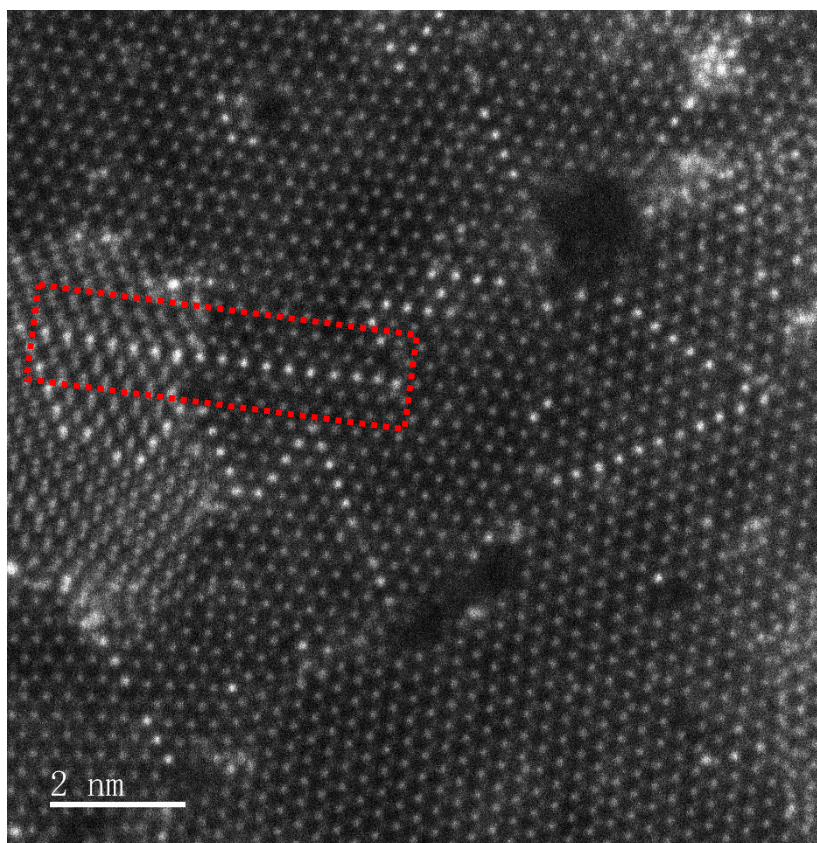
**Supplementary Fig. 9 | STEM investigation of Pt distribution in grain boundaries of small twist angle in MoS<sub>2</sub> nanograin films.** The Pt atoms randomly insert into the grain boundaries of MoS<sub>2</sub>.



**Supplementary Fig. 10** | Intensity profile along white lines in Fig. 2b-c. The simulated intensity profile vertical to Pt SMACs is consistent with that of the experimental result.



**Supplementary Fig. 11 | Atomic structure of vertex areas and joints of Pt SMACs. (A-C)** High magnification ADF-STEM images of joints of Pt SMACs. Mixed 4|6|8 rings are formed in these regions. **(D-E)** Detailed atomic configuration of vertex areas of intersecting Pt SMACs.



**Supplementary Fig. 12 | STEM investigation of Pt SMACs across monolayer and bilayer MoS<sub>2</sub>.** The Pt SMAC in the red rectangular region is embedded into the bottom layer of MoS<sub>2</sub>.

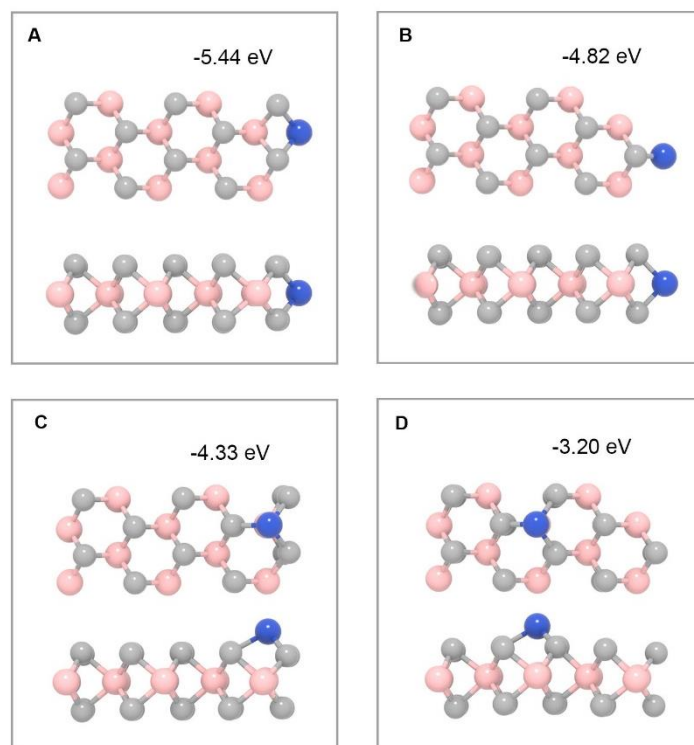
**Supplementary Table 1 | Raman spectra obtained from MoS<sub>2</sub> films.**

<b>Sample</b>	<b>E<sub>2g</sub> Peak Position (cm<sup>-1</sup>)</b>	<b>A<sub>1g</sub> Peak Position (cm<sup>-1</sup>)</b>	<b>E<sub>2g</sub> FWHM (cm<sup>-1</sup>)</b>	<b>I<sub>(E<sub>2g</sub>)/I<sub>(A<sub>1g</sub>)</sub></sub></b>
This work	384	405	19.0	0.34
Mechanical Exfoliation	383	404	6.9	1.42
CVD-growth	383	404	6.9	1.73

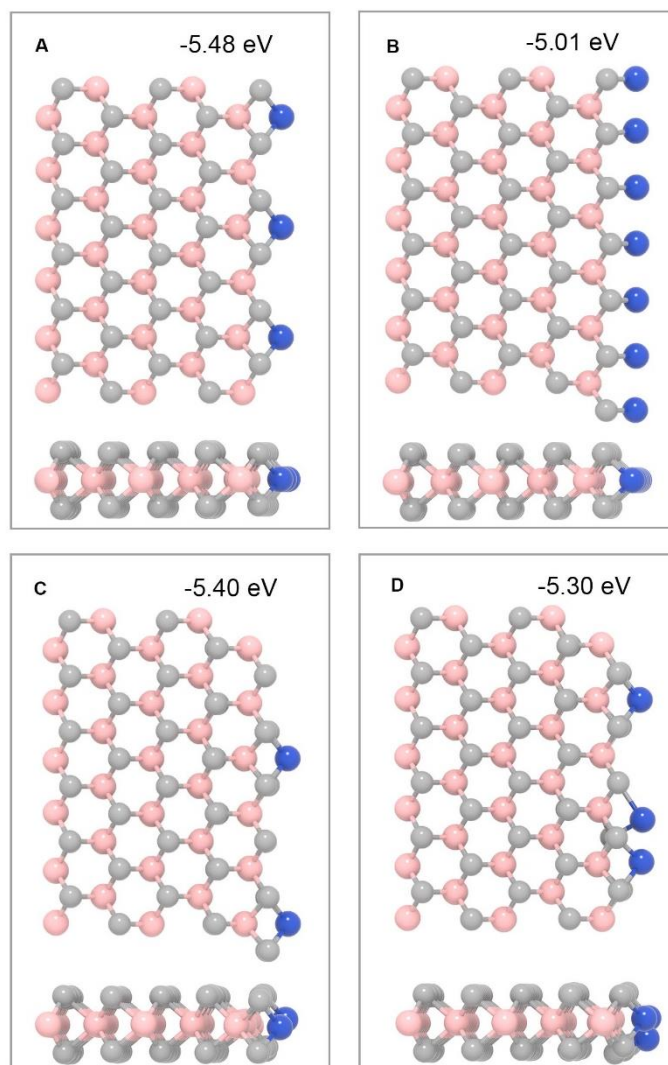
## **S2 Investigation of the possible growth mechanism**

### **2.1 Ab initio molecular dynamic (MD) simulations for Pt SMACs in bilayer MoS<sub>2</sub>**

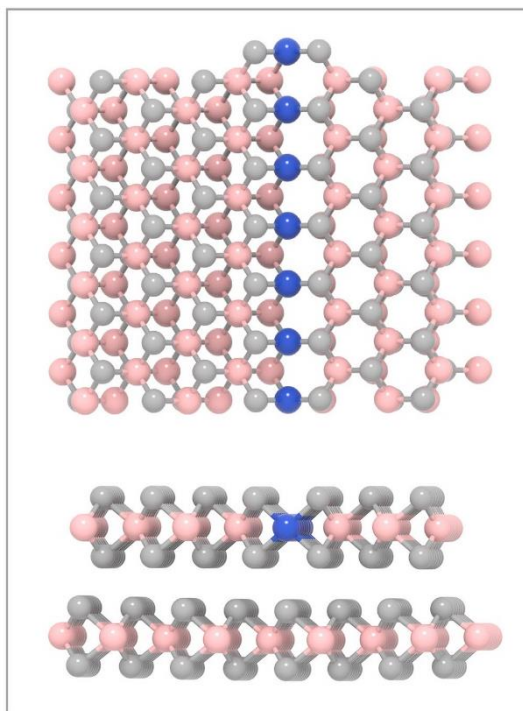
To construct bilayer MoS<sub>2</sub> model, we place the above model, MD model for Pt SMACs in monolayer MoS<sub>2</sub>, onto a perfect monolayer MoS<sub>2</sub>, with an arbitrary stacking angle. Interestingly, after optimization, Pt SMACs always on S atoms of the bottom layer with the layer spacing of 6.11 Å, which is slightly smaller than that of perfect bilayer MoS<sub>2</sub><sup>31</sup>. Meanwhile, MoS<sub>2</sub> forms 2H and 3R stacking registries on each side of Pt SMACs, respectively. We believe that Pt SMACs have a rotational alignment function here.



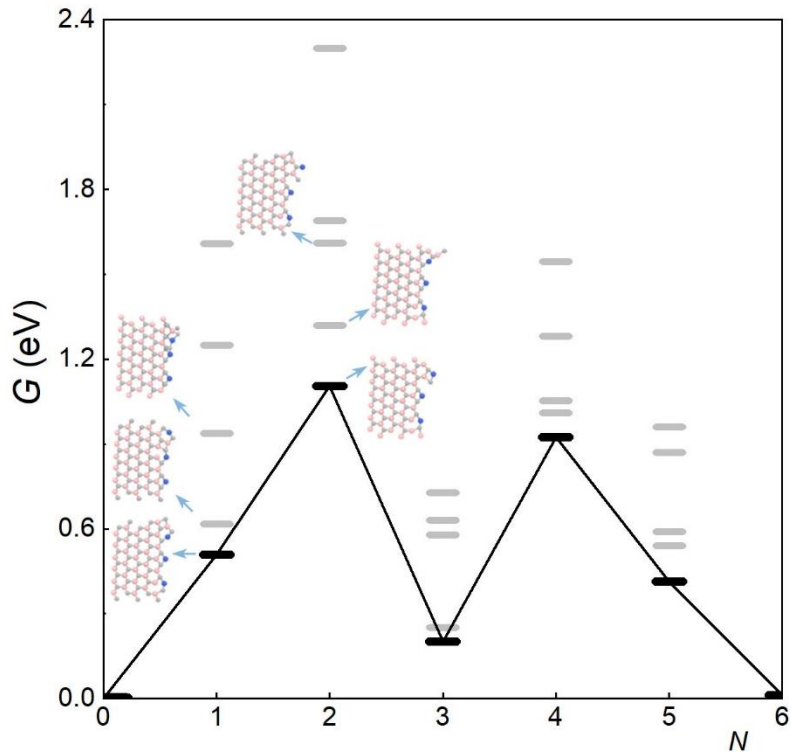
**Supplementary Fig. 13 | Binding energy of Pt atoms on monolayer MoS<sub>2</sub>.** Upper and lower panel represent top and side views of the adsorption model. Gray, pink, and blue spheres represent S, Mo, and Pt atoms, respectively. As demonstrated in (A), Pt has the lowest binding energy to form bonds with four S atoms at the edge of MoS<sub>2</sub>. That is, a single Pt atom tends to be chemically adsorbed at this site.



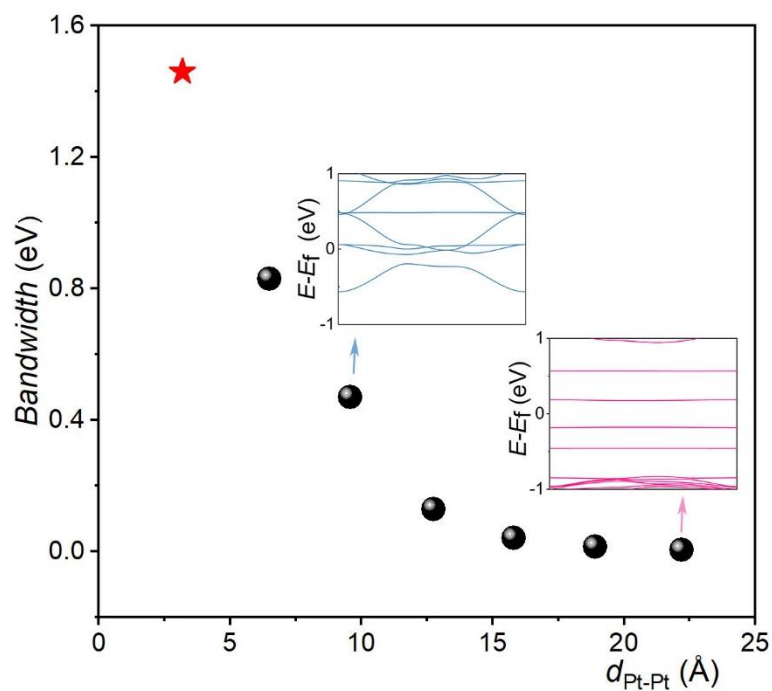
**Supplementary Fig. 14 | Formation energy of different Pt SMACs configuration in monolayer MoS<sub>2</sub> nanograin film.** As shown in (A), the consecutive Pt SMACs coordinated by 4 Pt-S bonds possess the lowest energy.



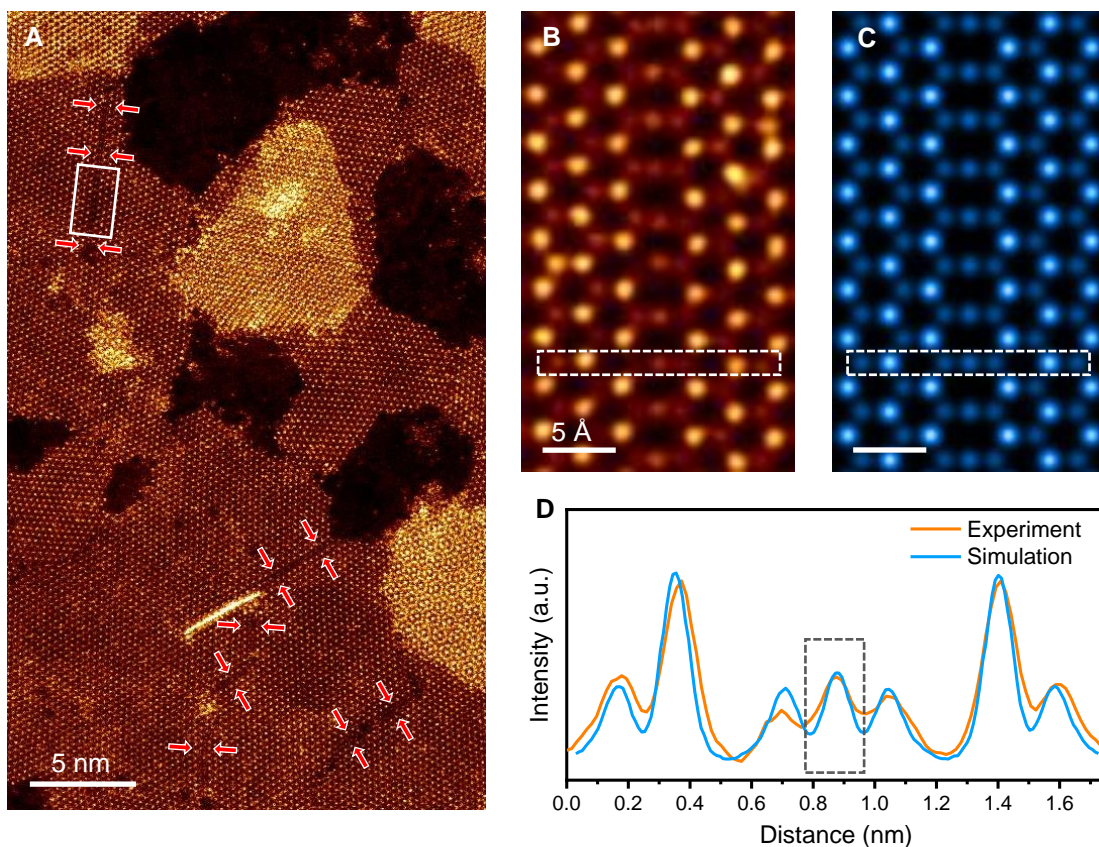
**Supplementary Fig. 15 | MD model for Pt SMACs in bilayer MoS<sub>2</sub> after structure optimization.**



**Supplementary Fig. 16 | The energy pathways for the kinetic growth along the Pt-passivated edge**, with the chemical potential  $\mu_{\text{MoS}_2} = 0 \text{ eV}$ . In detail, we add  $\text{MoS}_2$  unit step by step to the edge. At each step, we scanned a number of candidates structures whose energies are shown by gray bars, and determined the optimal configuration by comparing the system energy. These results confirm that the lowest energy pathway (the black line) seamlessly extends the  $\text{MoS}_2$  lattice, leaving the edge passivation unchanged. In particular, the edge growth manifests as the flow of kinks along the Pt-passivated edge, vividly like surfing on the waves.

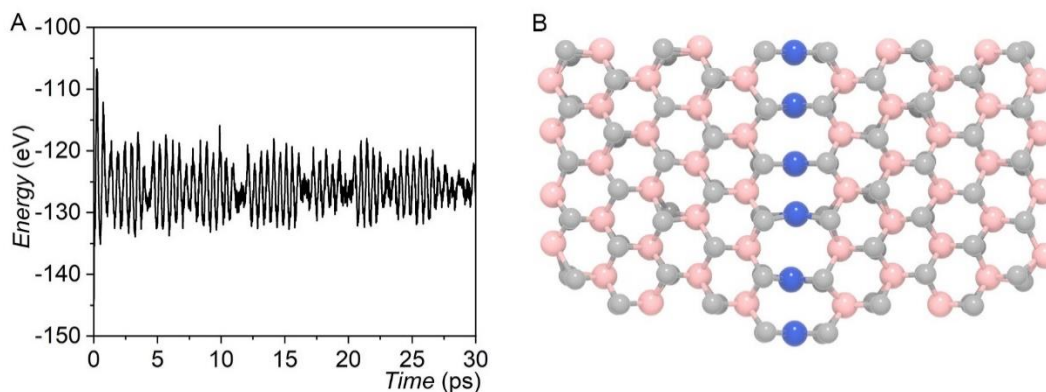


**Supplementary Fig. 17 | The widths of electronic bands derived from incorporated Pt atoms in MoS<sub>2</sub> as a function of the Pt-Pt spacing in the system. The red star represents the value of the Pt chain in our work. Insets show the magnified band structures near the Fermi level for the systems with a Pt-Pt spacing of 0.96 nm and 2.22 nm, respectively.**

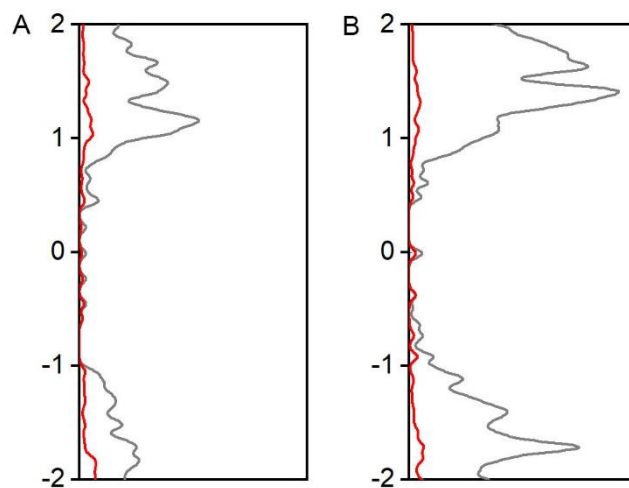


**Supplementary Fig. 18 | Co SMACs in MoS<sub>2</sub>.** (A) ADF-STEM images of Co SMACs in MoS<sub>2</sub> nanofilm. (B) Enlarged atomically resolution ADF-STEM images of the white rectangular area in (A). (C) Simulated ADF-STEM imaging of Co chain. (D) Intensity profile along white rectangular area in (B) and (C). The unusual low intensity marked by the grey frame in (D) is attributed to Co atom.

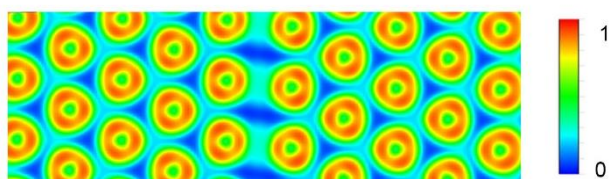
### S3 Electronic structure study and thermal stability investigation



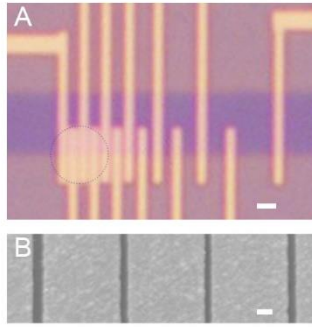
**Supplementary Fig. 19 | Thermal stability at 1000K.** (A) Total energy evolution of a MoS<sub>2</sub> system including a Pt atomic chain throughout a 30 ps AIMD simulation at 1000 K. (B) The system's structure at the end of the simulation. The Pt SMAC in MoS<sub>2</sub> structure does not undergo observable structural disruption at temperatures up to 1000 K throughout a 30-ps ab initio molecular dynamics simulation with a  $1 \times 5 \times 1$  supercell.



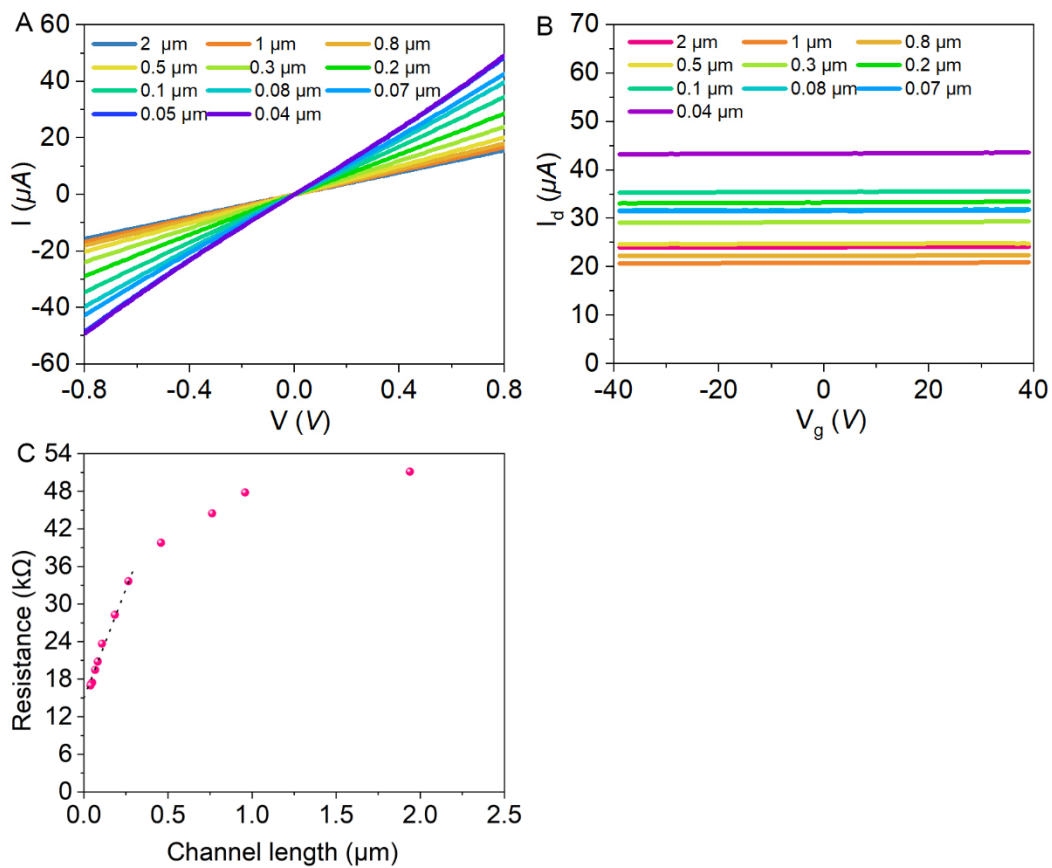
**Supplementary Fig. 20 | Projected density-of-states (PDOS).** PDOS of a Pt SMAC embedded in a monolayer (A) and bilayer (B) MoS<sub>2</sub>, corresponding to the band structure in Fig. 5a and 5b, respectively. Red lines mark the contribution of the Pt plus the S atoms directly bonded to them. The grey lines represent the whole Pt SMACs/MoS<sub>2</sub> system.



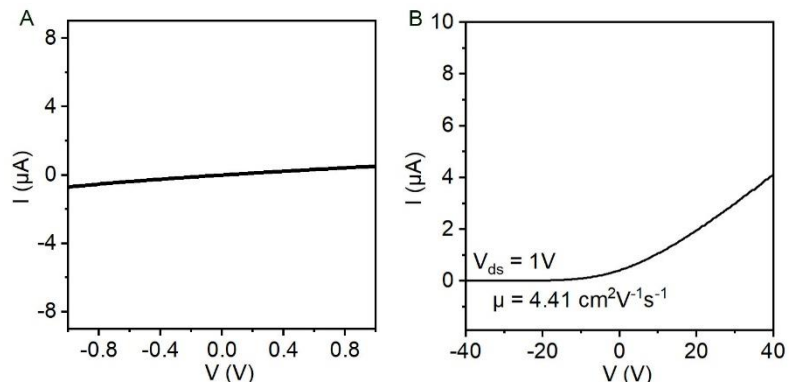
**Supplementary Fig. 21 | Electron localization function (ELF) map of Pt SMACs in a monolayer MoS<sub>2</sub> on the (001) plane.** Strong electronic localization can be observed between adjacent Pt and S atoms.



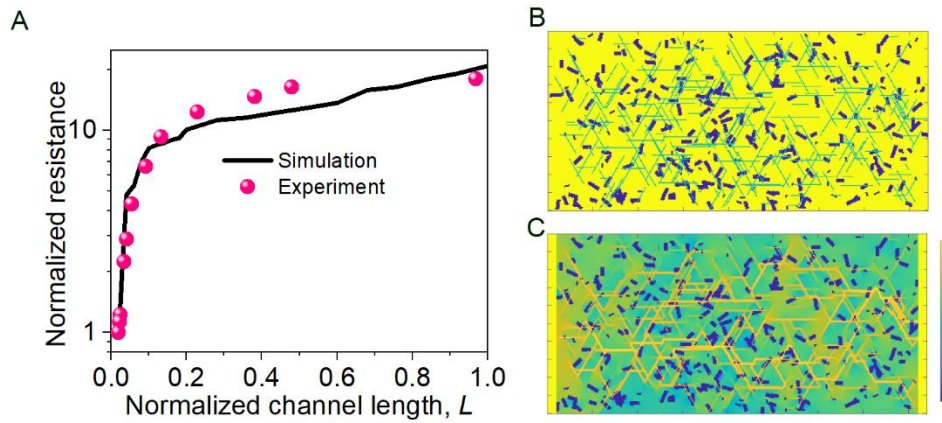
**Supplementary Fig. 22 | Optical microscope image (A) and zoom in SEM image (B) of FET devices in a TLM structure defined using e-beam lithography.** The scale bar is 1  $\mu\text{m}$  and 100 nm, respectively. The device structures with channel lengths from 2  $\mu\text{m}$  to 50 nm are fabricated, and the channel width is defined to be 1  $\mu\text{m}$ .



**Supplementary Fig. 23 | Electrical measurements** (A) I-V curves measured from FET devices with 1  $\mu\text{m}$  channel width and various channel lengths. (B) Transfer characteristic of Pt SMACs in MoS<sub>2</sub> films with different channel lengths at room temperature. (C) Total resistance versus channel length. The transmission-line measurement (TLM) result reveals a contact resistance ( $2R_c$ ) of 15  $\text{k}\Omega$  for Ti/Au electrodes on Pt SMACs in MoS<sub>2</sub> film.



**Supplementary Fig. 24 | FET performance of CVD-grown single crystal MoS<sub>2</sub> on SiO<sub>2</sub> substrate** (A) I-V curve of a bare MoS<sub>2</sub> FET device. (B) Transfer characteristics of the device. The device has a channel length of 4.7  $\mu\text{m}$ , and channel width of 10  $\mu\text{m}$ . The resistivity is calculated to be 3514  $\Omega\ \mu\text{m}$ .



**Supplementary Fig. 25 | Complex network modelling Pt SMAC inside MoS<sub>2</sub> film.** (A) Normalized simulated film resistivity and experimental results as a function of channel length. (B) Conductance map for Pt SMAC inside MoS<sub>2</sub> film with the largest channel length of  $L$  (normalized value of 1, corresponding to 2  $\mu\text{m}$  in the experiment). The cyan, yellow and blue regions correspond to  $R_{Pt\ SMAC}$ ,  $R_{MoS_2}$ , and  $R_{defect}$ , respectively. (C)  $\text{Log}_{10}|\text{current}|$  colour map calculated for the device in (B).

## Supplementary Notes

### Supplementary Note 1.

**Discussion of liquid Pt nanodroplets.** As shown in Supplementary Fig. 1, the employed Pt precursors have a diameter of 0.5-2 nm, with several nanometers of inter-particle spacing. Such a small size endows a significantly lower melting point, forming a liquid phase under our growth temperature (Fig. 1 e). These liquid Pt nanodroplets facilitate the mobility of Pt atoms during the growing process. To verify this behavior, we screen the preferred adsorption sites on MoS<sub>2</sub> for Pt atoms by calculations. Supplementary Fig. 11 shows the calculated binding energies of the Pt atom at different sites, indicating that the Pt atom has the lowest binding energy at the edge of MoS<sub>2</sub> and forms a Pt-S<sub>4</sub> motif with covalent bonds. *That is*, a single Pt atom tends to be chemically adsorbed at this edge site. This result agrees well with our STEM observations (Fig. 4a Inset), supporting "surfing at the growth front" for Pt atoms.

## Supplementary Note 2.

**Discussion on network conduction mechanism.** We employed complex-network-based modeling method to investigate carrier transport in our Pt SMAC network inner MoS<sub>2</sub> film (see details in method). In our model, the physical system was first converted into complex resistor network graphs by a universal discretization approach<sup>6</sup>. By solving the Kirchhoff's current law and Ohm's law, we can obtain the overall resistance and current distribution of the system (Fig. 5g-h, Supplementary Fig. 24).

We model the system by introducing conductive atomic chains into a resistive matrix of MoS<sub>2</sub>. The chains are oriented in a 3-fold symmetry with random overlap, which attempts to model the effect of atomic chains located at the mirror twin boundaries of MoS<sub>2</sub> in our sample (Supplementary Fig. 24b). The calculated film resistivity demonstrates a similar  $l$  dependence, well-consistent with the experimental results (Fig. 5h). To further explore this phenomenon, the current distribution was computed (Fig. 5g). It is evident that carrier conduction proceeds by percolation through the Pt atomic chains for all length scales. At short channel lengths (region 1), an increase in resistivity occurs due to the termination of critical conduction pathways as expected for conventional percolation. However, at longer channel lengths (region 2), the effect of the 3-fold symmetry can be observed: When several MoS<sub>2</sub> grains merge, the atomic chains form Y-shaped connections where one conduction pathway is split into two. These Y-junctions increase the chance of forming a critical conduction pathway two-fold compared to a linear orientation. This hierarchical conduction process modifies the percolation condition, and each Y junction enhances the conductivity of the channel.

### Supplementary Note 3.

**Discussion on the controllability of Pt SMACs.** The achieved high reproducibility of Pt SMACs is due to the optimized growth conditions. We found that the key three factors are the growth temperature, substrate effect, and Pt precursor:

1. **Growth temperature.** In our experiment, a Pt SMACs network inside MoS<sub>2</sub> film can be well-obtained at 650 °C (Supplementary Fig. 4d). In contrast, Pt single atoms in amorphous MoS<sub>2</sub> film are obtained at a temperature below 600 °C (Supplementary Fig. 4a), and PtS<sub>x</sub> nanoparticles form at above 750 °C (Supplementary Fig. 4b).
2. **Substrate effect.** Additionally, we studied the substrate effect. For example, sapphire substrate tends to promote the formation of single dispersed Pt atoms (Supplementary Fig. 4e-f), in sharp contrast with Pt chains on SiO<sub>2</sub>/Si substrate (Supplementary Fig. 4d).
3. **Pt precursor.** Thanks to a low deposition rate (0.1 Å s<sup>-1</sup>), a low substrate temperature (18 °C), and a high-vacuum pressure (10<sup>-9</sup> torr), the monodispersed single Pt atom/nanoclusters can be achieved in our experiment. Further, their sizes and amounts can be precisely controlled by varying the deposition time (Supplementary Fig. 2). An optimized deposition time (10 s) would lead to a high-dense Pt SMACs network inside MoS<sub>2</sub> film with ultra-high average loading mass of atomically dispersed Pt over 10 wt% (Supplementary Fig. 4d). A further increase of the Pt deposition time results in a large number of isolated Pt nanoparticles (Supplementary Fig. 4c).

Noteworthy, the chemical co-deposition method is successfully extended to the synthesis of Co SMACs (Supplementary Fig. 18).

## S4 References

1. Zhang, Q., Zhang, L., Jin, C., Wang, Y. & Lin, F. CalAtom: A software for quantitatively analysing atomic columns in a transmission electron microscope image. *Ultramicroscopy* **202**, 114-120 (2019).
2. Bruix, A. *et al.* Maximum noble-metal efficiency in catalytic materials: atomically dispersed surface platinum. *Angew. Chem. Int. Ed.* **53**, 10525-10530 (2014).
3. Cheng, N. *et al.* Platinum single-atom and cluster catalysis of the hydrogen evolution reaction. *Nat. Commun.* **7**, 1-9 (2016).
4. Deng, J. *et al.* Triggering the electrocatalytic hydrogen evolution activity of the inert two-dimensional MoS<sub>2</sub> surface via single-atom metal doping. *Energy Environ. Sci.* **8**, 1594-1601 (2015).
5. Lang, R. *et al.* Non defect-stabilized thermally stable single-atom catalyst. *Nat. Commun.* **10**, 1-10 (2019).
6. Li, H. *et al.* Synergetic interaction between neighbouring platinum monomers in CO<sub>2</sub> hydrogenation. *Nat. Nanotechnol.* **13**, 411-417 (2018).
7. Li, X. *et al.* Single-atom Pt as co-catalyst for enhanced photocatalytic H<sub>2</sub> evolution. *Adv. Mater.* **28**, 2427-2431 (2016).
8. Liu, L. *et al.* Generation of subnanometric platinum with high stability during transformation of a 2D zeolite into 3D. *Nat. Mater.* **16**, 132-138 (2017).
9. Qiao, B. *et al.* Single-atom catalysis of CO oxidation using Pt<sub>1</sub>/FeO<sub>x</sub>. *Nat. Chem.* **3**, 634 (2011).
10. Ding, K. *et al.* Identification of active sites in CO oxidation and water-gas shift over supported Pt catalysts. *science* **350**, 189-192 (2015).
11. Yang, S., Kim, J., Tak, Y. J., Soon, A. & Lee, H. Single-atom catalyst of platinum supported on titanium nitride for selective electrochemical reactions. *Angew. Chem. Int. Ed.* **55**, 2058-2062 (2016).
12. Coelho, P. M. *et al.* Post-synthesis modifications of two-dimensional MoSe<sub>2</sub> or MoTe<sub>2</sub> by incorporation of excess metal atoms into the crystal structure. *ACS nano* **12**, 3975-3984 (2018).
13. Liu, J. *et al.* High performance platinum single atom electrocatalyst for oxygen reduction reaction. *Nat. Commun.* **8**, 1-10 (2017).
14. Zhang, L., Han, L., Liu, H., Liu, X. & Luo, J. Potential-cycling synthesis of single platinum atoms for efficient hydrogen evolution in neutral media. *Angew. Chem. Int. Ed.* **56**, 13694-13698 (2017).
15. Wang, L. *et al.* A sulfur-tethering synthesis strategy toward high-loading atomically dispersed noble metal catalysts. *Science advances* **5**, eaax6322 (2019).
16. Zhang, H. *et al.* Dynamic traction of lattice-confined platinum atoms into mesoporous carbon matrix for hydrogen evolution reaction. *Science advances* **4**, eaao6657 (2018).
17. Zhang, J. *et al.* Single platinum atoms immobilized on an MXene as an efficient catalyst for the hydrogen evolution reaction. *Nature Catalysis* **1**, 985-992 (2018).
18. Zhang, J. *et al.* Cation vacancy stabilization of single-atomic-site Pt<sub>1</sub>/Ni(OH)<sub>x</sub> catalyst for diboration of alkynes and alkenes. *Nat. Commun.* **9**, 1-8 (2018).
19. Zhang, Z. *et al.* Thermally stable single atom Pt/m-Al<sub>2</sub>O<sub>3</sub> for selective hydrogenation and CO oxidation. *Nat. Commun.* **8**, 1-10 (2017).
20. Lin, L. *et al.* Low-temperature hydrogen production from water and methanol using Pt/ $\alpha$ -MoC catalysts. *Nature* **544**, 80-83 (2017).
21. Wei, H. *et al.* Iced photochemical reduction to synthesize atomically dispersed metals by suppressing nanocrystal growth. *Nat. Commun.* **8**, 1-8 (2017).
22. Zhang, B. *et al.* Stabilizing a platinum<sub>1</sub> single-atom catalyst on supported

- phosphomolybdic acid without compromising hydrogenation activity. *Angew. Chem. Int. Ed.* **55**, 8319-8323 (2016).
23. Kim, J. *et al.* Highly durable platinum single-atom alloy catalyst for electrochemical reactions. *Adv. Energy Mater.* **8**, 1701476 (2018).
  24. Zeng, X. *et al.* Single-Atom to Single-Atom Grafting of Pt<sub>1</sub> onto Fe-N<sub>4</sub> Center: Pt<sub>1</sub>@ Fe-N-C Multifunctional Electrocatalyst with Significantly Enhanced Properties. *Adv. Energy Mater.* **8**, 1701345 (2018).
  25. Chen, Y. *et al.* Identifying size effects of Pt as single atoms and nanoparticles supported on FeO<sub>x</sub> for the water-gas shift reaction. *ACS Catal.* **8**, 859-868 (2018).
  26. Zeng, Q. *et al.* Highly anisotropic thermoelectric properties of black phosphorus crystals. *2D Materials* **6**, 045009 (2019).
  27. Zhao, D. *et al.* MXene (Ti<sub>3</sub>C<sub>2</sub>) vacancy-confined single-atom catalyst for efficient functionalization of CO<sub>2</sub>. *J. Am. Chem. Soc.* **141**, 4086-4093 (2019).
  28. Ye, S. *et al.* Highly stable single Pt atomic sites anchored on aniline-stacked graphene for hydrogen evolution reaction. *Energy Environ. Sci.* **12**, 1000-1007 (2019).
  29. Li, T., Liu, J., Song, Y. & Wang, F. Photochemical solid-phase synthesis of platinum single atoms on nitrogen-doped carbon with high loading as bifunctional catalysts for hydrogen evolution and oxygen reduction reactions. *ACS Catal.* **8**, 8450-8458 (2018).
  30. Zhu, Y. *et al.* One-pot pyrolysis to N-doped graphene with high-density Pt single atomic sites as heterogeneous catalyst for alkene hydrosilylation. *ACS Catal.* **8**, 10004-10011 (2018).
  31. He, J., Hummer, K. & Franchini, C. Stacking effects on the electronic and optical properties of bilayer transition metal dichalcogenides MoS<sub>2</sub>, MoSe<sub>2</sub>, WS<sub>2</sub>, and WSe<sub>2</sub>. *Phys. Rev. B* **89**, 075409 (2014).